



# Effect of Ag layer thickness on optical and electrical properties of ion-beam-sputtered TiO<sub>2</sub>/Ag/TiO<sub>2</sub> multilayer thin film

Rajan Singh<sup>1</sup>, Mukul Gupta<sup>2</sup>, and S. K. Mukherjee<sup>1,\*</sup>

<sup>1</sup>Department of Physics, Birla Institute of Technology, Mesra, Ranchi 835215, India

<sup>2</sup>UGC-DAE Consortium for Scientific Research, University Campus, Khandwa Road, Indore 45200, India

Received: 25 October 2021

Accepted: 29 January 2022

Published online:

11 February 2022

© The Author(s), under exclusive licence to Springer Science+Business Media, LLC, part of Springer Nature 2022

## ABSTRACT

TiO<sub>2</sub>/Ag/TiO<sub>2</sub> multilayer films have been deposited by Ion-beam sputtering technique with different Ag thickness. X-ray reflectivity technique with 3-layer fitting model has been used to calculate thickness, density, and roughness of the multilayer films. Gaussian fitting of XRD and Raman data is used to detect the crystalline growth of films while FTIR data confirm the presence of metal layer in the films. A phonon confinement effect originating from decrease in crystallite size is also observed with blue shift in some of the Raman active modes. Effect of Ag layer thickness on optical and electrical properties of multilayer films has been presented including a comparative study of our data with previously reported work on TiO<sub>2</sub>/Ag/TiO<sub>2</sub> transparent conducting oxides. Transmittance of multilayer films in visible region (550 nm) has increased from 65 to 81% with increase in Ag thickness. The band gaps calculated from Tauc plot of these films follow Burstein–Moss effect. Sheet resistance has decreased from 15.41 to 5.92 Ω/□ while carrier concentration and mobility show an increasing trend from  $5.94 \times 10^{21}$  to  $1.35 \times 10^{22}$  and 6.83 to 13.72 cm<sup>2</sup>/Vs, respectively, with the increase in Ag mid-layer thickness. Haacke's Figure of Merit (FOM) is recorded to be  $7.9 \times 10^{-3} \Omega^{-1}$ .

## 1 Introduction

Transparent conducting oxides (TCOs) have attracted huge attention in thin film development area due to its wide applications including solar cells, optoelectronic devices, sensors, LCDs, and LEDs. A variety of metal oxides like TiO<sub>2</sub>, ZnO, SnO<sub>2</sub>, and Nb<sub>2</sub>O<sub>5</sub> have been extensively exploited for developing efficient

TCOs. In later phases, these are even doped with Al-, Nb-, Ga-like materials for enhanced electrical and optical properties. In order to replace ITO films for its toxic nature and cost ineffective reasons, metal oxides like TiO<sub>2</sub> and ZnO have been widely investigated and found promising results. TiO<sub>2</sub> have been studied for various applications due to their chemical stability, high photosensitivity, high photocatalytic activity,

Address correspondence to E-mail: sanat\_aphy@yahoo.co.in

and low toxicity [1]. Also,  $\text{TiO}_2$  has wide band gap ( $> 3$  eV) and high refractive index, which makes it highly photoactive in the UV region and an efficient solar cell material [2, 3].

In recent development, multilayer thin films have been a great area of interest compared to single-layer TCOs due to its improved optical and electrical behavior. Multilayer TCO has a combination of thin metal layer sandwiched between different metal oxide layers (dielectrics). The thickness ratio of dielectric and metal layer plays an important role in electrical and optical properties of the film.  $\text{TiO}_2$  is a desired dielectric material for multilayer films due to its wide band gap, high refractive index (2.7), high transparency in visible region, and better chemical stability. Ag is preferred as middle layer in oxide/metal/oxide (O/M/O) because it results in low sheet resistance and high transmittance in visible region. The variable Ag thickness is important in finding the optimum electrical and optical balance of TCO for industrial application.

The precise thickness variation of mid-layer ranging within few nanometers is challenging and requires much controlled film growth. Although various sputtering methods, such as direct current (DC) magnetron sputtering and radio frequency (RF) magnetron sputtering, are used to develop  $\text{TiO}_2/\text{Ag}/\text{TiO}_2$  multilayer TCOs, ion-beam sputtering (IBS) has many advantages over others. It uses a high-energy ion-beam source over the sputtering target which produces a dense material on substrate resulting into high refractive index compared to other deposition techniques. The scattering loss is much lower for ion-beam-sputtered films than using other methods [3]. It also provides better control over deposition parameters like current density and energy of source ion beam, for desired growth of films.

This work has demonstrated the development of  $\text{TiO}_2/\text{Ag}/\text{TiO}_2$  multilayer thin films with variation in Ag layer thickness. A comparative analysis of electrical and optical properties of the developed TCOs with previous work has been presented.

## 2 Experimental details

$\text{TiO}_2/\text{Ag}/\text{TiO}_2$  multilayer thin films were deposited on quartz and Si (100) substrates using Ion-beam sputtering system (IBS) consisting of hot-cathode Kaufman type 1.5 kV gridded ion source. Titanium

target (99.99%) of size  $100 \times 100 \times 1$  mm was used with similar dimension of silver target (99.99%). Oxygen and argon gases were used during the sputtering process. The base pressure inside the chamber was  $2 \times 10^{-5}$  Pa, while the working pressure was  $2 \times 10^{-3}$  Pa. Ti and Ag targets were bombarded with ion beam with beam current of 30 mA and 1000 eV ion-beam energy. Depending upon the deposition rate of  $\text{TiO}_2$  and Ag, the precise sputtering time for both the targets was assigned alternately to obtain the multilayer film with desired thickness (Table 1).  $\text{TiO}_2$  thickness of both the upper and lower layer was fixed at 30 nm while Ag (middle layer) thickness was varied at 2 nm, 4 nm, and 8 nm. The samples were named TAT A (single-layer  $\text{TiO}_2$ —60 nm), TAT B ( $\text{TiO}_2$ —30 nm/Ag—2 nm/ $\text{TiO}_2$ —30 nm), TAT C ( $\text{TiO}_2$ —30 nm/Ag—4 nm/ $\text{TiO}_2$ —30 nm), and TAT D ( $\text{TiO}_2$ —30 nm/Ag—8 nm/ $\text{TiO}_2$ —30 nm). After the deposition, TAT films were annealed at 500 °C in a high vacuum environment.

X-ray reflectivity (XRR) measurement was performed on multilayer films between 2 and 5° with step size of 0.01° using Bruker D8 Discover diffractometer with  $\text{CuK}\alpha$  (0.154 nm) source. Parratt32 software was used for XRR data fitting and calculations of thickness, density, and roughness of the multilayer films. Crystallographic properties were analyzed using Bruker D8 Advanced X-ray diffractometer (XRD). Scanning electron microscope (SEM) and energy-dispersive X-ray (EDX) data were obtained by field emission scanning electron microscope (FESEM, Sigma 300, Carl Zeiss Microscope Ltd., Germany) operated at 20 kV. UV–Visible spectra of multilayer films were carried in transmission mode using Lambda 20, PerkinElmer UV–Visible spectrometer. Raman modes were identified using Renishaw Invia Raman spectrometer (514.6 nm Ar laser) across  $100$ – $1000$   $\text{cm}^{-1}$ . Fourier transformed infrared (FTIR) analysis was done using PerkinElmer Frontier spectrometer across  $400$ – $4000$   $\text{cm}^{-1}$ . Hall

**Table 1**  $\text{TiO}_2/\text{Ag}/\text{TiO}_2$  multilayer deposition parameters

| Sample  | $\text{O}_2$ (sccm) | Deposition time (min.) |
|---|---------------------|------------------------|
| TAT A ( $\text{TiO}_2$ )                        | 2.5                 | 42.52                  |
| TAT B ( $\text{TiO}_2/\text{Ag}/\text{TiO}_2$ ) | 2.5                 | 21.26/0.20/21.26       |
| TAT C ( $\text{TiO}_2/\text{Ag}/\text{TiO}_2$ ) | 2.5                 | 21.26/0.39/21.26       |
| TAT D ( $\text{TiO}_2/\text{Ag}/\text{TiO}_2$ ) | 2.5                 | 21.26/0.77/21.26       |

measurement was done by Van der Pauw's method using four-point probe technique. Keithley 2400 sourcemeter was used during the hall measurements with magnetic field of 1 Tesla.

### 3 Result and discussion

#### 3.1 XRR

X-ray reflectivity is a powerful non-destructive technique to calculate the thickness, density, and roughness of thin films through electron density profile as a function of depth. Figure 1 represents the 3D schematic diagram of TiO<sub>2</sub> and TiO<sub>2</sub>/Ag/TiO<sub>2</sub> multilayer films with different Ag thickness. Figure 2a depicts schematic diagram of interaction of X-rays with multilayer films in terms of reflectivity and momentum transfer. The reflected X-rays at each surface create interference fringes (Kiessig fringes) with numerous oscillations resulting into a reflectometry pattern. Thickness of the multilayer film is related to Bragg's law as

$$n\lambda = 2(d_1 \sin \alpha_{i1} + d_2 \sin \alpha_{i2} + d_3 \sin \alpha_{i3}), \quad (1)$$

where,  $d_1$ ,  $d_2$ , and  $d_3$  are thickness of different layers of film. In XRR technique, a monochromatic beam of X-ray ( $\alpha_i$ ) is incident on thin film surface and reflected at  $\alpha_f$  with wave vector  $k_i$  and  $k_f$ , respectively. The momentum transfer along the surface normal ( $z$ ) is given by [4, 5]

$$Q_z = k_f - k_i = \frac{4\pi}{\lambda} \sin \alpha_i, \quad (2)$$

where  $\lambda$  is the X-ray wavelength.

Figure 2b depicts the X-ray reflectivity profile of TiO<sub>2</sub>/Ag/TiO<sub>2</sub> multilayer films along with TiO<sub>2</sub> monolayer. The reflectivity curve was fitted with theoretical model of independent TiO<sub>2</sub>, Ag, and H<sub>2</sub>O adsorbate layers using parratt32 software [6, 7]. A good fitting of reflectivity curve with appropriate theoretical model results in precise thickness

determination of different layers. Critical angle ( $\theta_c$ ) is an important parameter for calculating electron density and mass density. In our experiment, critical angle ranged between 0.52 and 0.55° while the critical momentum transfer ( $Q_c$ ) was observed to be 0.035–0.04 Å<sup>-1</sup> for TiO<sub>2</sub>/Ag/TiO<sub>2</sub> multilayer films. Singh et al. (2019) have described the elaborated theoretical model to calculate the density and roughness of thin film [6]. Upon applying best suitable theoretical fitting model and calculations, the thickness, density, and roughness of our TiO<sub>2</sub>/Ag/TiO<sub>2</sub> multilayer films are presented in Table 2. Based on these data it was observed that, with the increase in Ag mid-layer thickness, density, and roughness of multilayer films also increased substantially.

#### 3.2 XRD

XRD spectra of TiO<sub>2</sub>/Ag/TiO<sub>2</sub> multilayer films with different Ag thickness (0–8 nm) are depicted in Fig. 3. Peaks were fitted with Gaussian profile to determine peak position, FWHM, and intensity. Table 3 shows the crystallite size, micro-strain, and dislocation density of multilayer films. The crystallite size was determined using Scherrer formula and the micro-strain was calculated using Williamson–Hall equation [8, 9]. The inset image in Fig. 3 represents the magnified version of TiO<sub>2</sub> and Ag peaks (35–58°) of TAT D multilayer spectra for better view and analysis. Upon deconvolution with Gaussian profile fitting, it was observed that all films were crystalline in nature. The diffracted peaks at  $2\theta$  values 26.52°, 37.98°, and 54.35° refer to TiO<sub>2</sub> anatase (JCPDS 84-1286) crystal planes (101), (004), and (211), respectively. Few low intensity yet prominent peaks of Ag were observed at 43.98°, 64.26°, and 77.18° in some of the films. These peaks correspond to (200), (220), and (311) planes, respectively (JCPDS 04-0783). TAT A contains only anatase (101) peaks, whereas TAT B, TAT C, and TAT D confirm the presence of both TiO<sub>2</sub> and Ag. With the increase in Ag thickness, the intensity of peaks increases along with improved

**Fig. 1** 3D diagram depicting TiO<sub>2</sub>/Ag/TiO<sub>2</sub> multilayer film with different Ag thickness



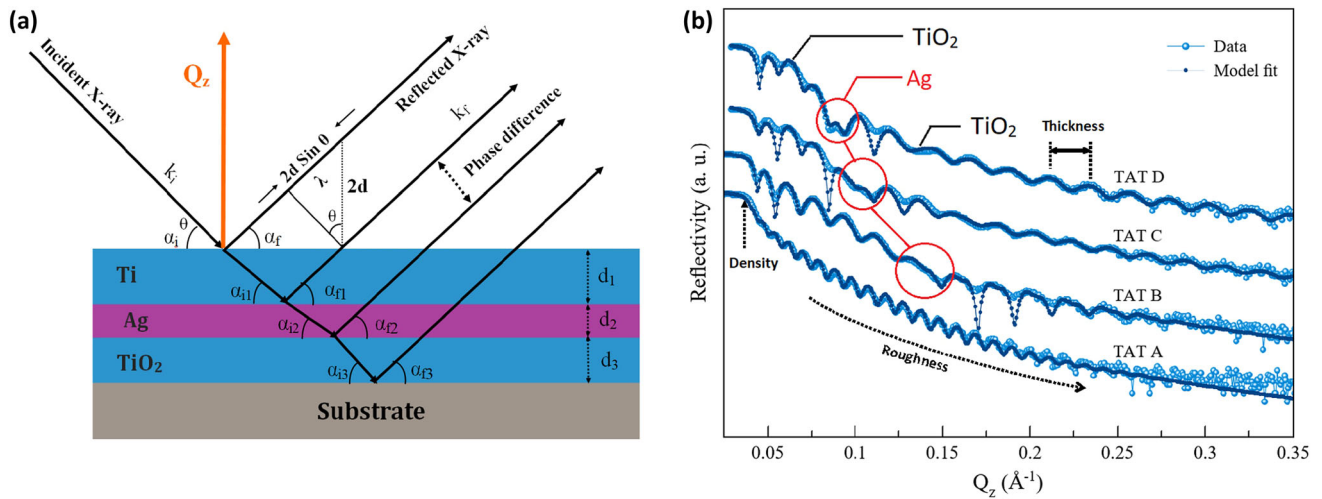


**Fig. 2** (a) Schematic diagram presenting interaction of x-rays with different layers of film. (b) Electron density profile of TiO<sub>2</sub>/Ag/TiO<sub>2</sub> multilayer with appropriate fitting model. Ag reflectivity curve is clearly visible (red circle) between the two TiO<sub>2</sub> curves

**Table 2** Thickness, density, and roughness of TiO<sub>2</sub>/Ag/TiO<sub>2</sub> multilayer films

| Sample | Layer thickness (nm) | Density (g/cm <sup>3</sup> ) | Roughness (nm) |
|--------|----------------------|------------------------------|----------------|
| TAT A  | 60                   | 3.75                         | 0.9            |
| TAT B  | 30/2/30              | 4.01/9.1/4.05                | 1.2/1.1/1.8    |
| TAT C  | 30/4/30              | 4.54/10.9/4.56               | 1.4/1.9/1.8    |
| TAT D  | 30/8/30              | 4.61/11.4/4.59               | 1.5/2.0/2.2    |

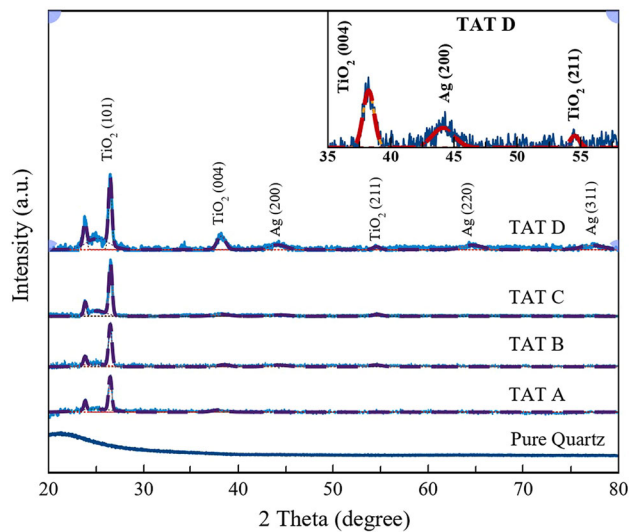


**Fig. 3** XRD spectra of TiO<sub>2</sub>/Ag/TiO<sub>2</sub> multilayer films. Crystalline TiO<sub>2</sub> with anatase phase is observed along with Ag peaks

crystallinity of multilayer films [10, 11]. The preferential growth of crystalline TiO<sub>2</sub> structure occurs in the direction (101) plane and Ag grows in (200) plane.

The peak at 23.88° cannot be indexed as it neither matches with any of the TiO<sub>2</sub> phases nor with Ag nor

any of their mixed phases. Quartz do have a peak at a similar location. However, such a peak does not appear in the XRD profile of our quartz substrate (see Fig. 3). Quartz substrate is well known to have induced lattice mismatch against the deposited film giving rise to high lattice strain [12]. This is an important factor in thin film crystalline growth as high lattice strain may lead to crystal defects and dislocations. Increase in film thickness reduces the strength of strain in the films [13].

Apart from crystal dislocations, crystallite size plays major role in induced lattice strain in thin films due to grain boundary effect. When crystallite size decreases, the stress caused by internal surface tension induces lattice strain. However, when crystallite size increases, the lattice strain becomes weak due to lower stress field from grain boundaries [14]. The crystallite size of the multilayer films depicts similar behavior with the increase in Ag thickness. As the crystallite size increases from ~ 11 to 19 nm, a decrease in micro-strain from  $1.27 \times 10^{-2}$  to  $1.03 \times 10^{-2}$  is observed. Dislocation density, which indicates the amount of defects in the films, is seen to be decreasing with the increase in Ag thickness. This

**Table 3** Average crystallite size, micro-strain, and dislocation density of TiO<sub>2</sub>/Ag/TiO<sub>2</sub> multilayer films

| Sample | Average Crystallite size (nm) |     | Micro-strain<br>(10 <sup>-2</sup> ) | Dislocation density<br>(10 <sup>11</sup> /cm <sup>2</sup> ) |
|--------|-------------------------------|-----|-------------------------------------|---|
|        | TiO <sub>2</sub>              | Ag  |                                     |   |
| TAT A  | 11.1                          | –   | –                                   | 8.1   |
| TAT B  | 13.2                          | 4.5 | 1.27                                | 5.7   |
| TAT C  | 14.5                          | 5.9 | 1.16                                | 4.8   |
| TAT D  | 19                            | 7.5 | 1.03                                | 2.8   |

shows that TAT D multilayer film with 8 nm Ag thickness has fewer defects compared to other films.

### 3.3 FESEM/EDX

FESEM images of TiO<sub>2</sub>/Ag/TiO<sub>2</sub> multilayer films are shown in Fig. 4. Microstructure of all the films are smooth, dense, and free from cracks. Pure TiO<sub>2</sub> and Ag (2 nm) film do not show much difference in surface morphology. Ag (4 nm) film looks more dense and shows slight agglomeration on the surface. Some dark spots are visible which appears due to Ag agglomeration over the TiO<sub>2</sub> surface, forming island-like structure confirming the Volmer–Weber model of multilayer films [15, 16]. These island agglomerate in Ag (8 nm) film, thereby, forming a continuous layer. Inset image of Fig. 4d represents the crystallite size of TAT D films using imageJ software. The average crystallite size is ~ 20 nm which is close to the values calculated by XRD spectra using Scherrer formula.

EDX compositional analysis of multilayer films is presented in Fig. 5. The elemental composition of films shows the presence of both Ti and Ag in multilayer films along with Si substrate due to high-energy EDX ion beam penetrating into the Si substrate. The wt% of Ag increases from 0.2 to 0.7% confirming the increase in Ag thickness in subsequent multilayers. The overall composition of Ag in TiO<sub>2</sub>/Ag/TiO<sub>2</sub> Multilayer films ranges between 2.5 and 10.3 wt% which is close to the expected value of Ag composition in multilayer by volume from 3.2 to 11.7% [17].

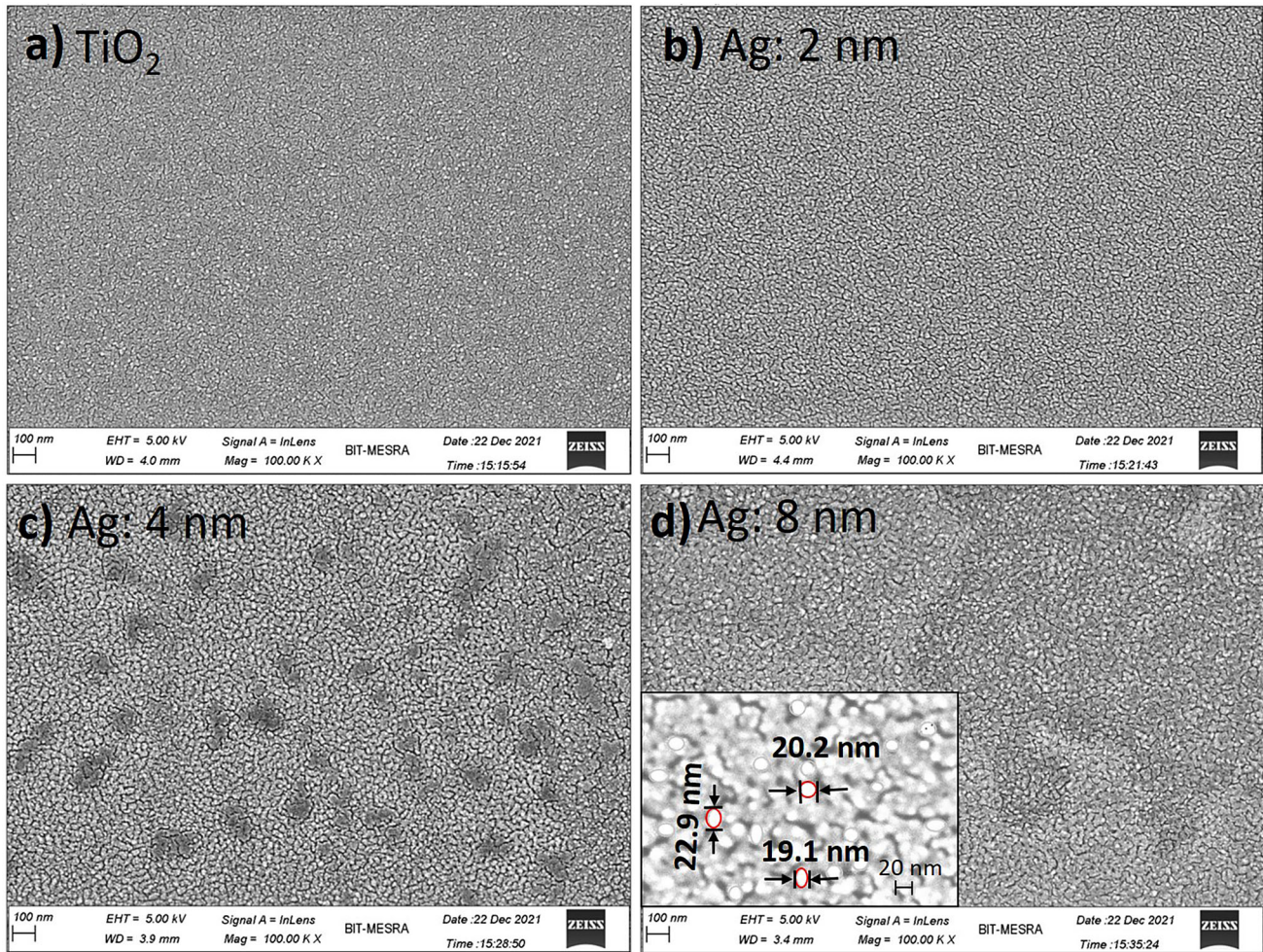
### 3.4 Raman

Figure 6 presents micro-Raman analyses of TiO<sub>2</sub>/Ag/TiO<sub>2</sub> multilayer films performed over 100–800 cm<sup>-1</sup> to obtain the vibrational modes present in samples. Raman spectra were fitted with Gaussian profile to obtain peak positions, FWHM, intensity, and area under the peak. TiO<sub>2</sub> anatase has six active

Raman modes: 1A<sub>1g</sub>, 2B<sub>1g</sub>, and 3E<sub>g</sub>. The Raman shifts observed at 144 cm<sup>-1</sup> (E<sub>g</sub>), 197 cm<sup>-1</sup> (E<sub>g</sub>), 395 cm<sup>-1</sup> (B<sub>1g</sub>), 515 cm<sup>-1</sup> (A<sub>1g</sub>/B<sub>1g</sub>), and 636 cm<sup>-1</sup> (E<sub>g</sub>) correspond to the characteristic peaks of tetragonal TiO<sub>2</sub> anatase phase [18, 19]. The active mode E<sub>g</sub> (144 cm<sup>-1</sup>, 395 cm<sup>-1</sup>, and 636 cm<sup>-1</sup>) refers to O–Ti–O symmetric stretching vibrations, B<sub>1g</sub> (395 cm<sup>-1</sup> and 515 cm<sup>-1</sup>) relates to O–Ti–O symmetric bending vibrations, and A<sub>1g</sub> (519 cm<sup>-1</sup>) refers to anti-symmetric bending vibrations in anatase lattice [20]. B<sub>1g</sub> (395 cm<sup>-1</sup>) is not observed in TAT A monolayer but present in subsequent multilayers while B<sub>1g</sub> (515 cm<sup>-1</sup>) is slightly red shifted in TAT A. There is a blue shift observed in E<sub>g</sub> (multilayers) which may occur due to non-stoichiometry and phonon confinement effect [21]. This effect can be related to the decrease in crystallite size in multilayers as explained in XRD results. A red shift in B<sub>1g</sub> mode is also observed in multilayer films suggesting distortion in TiO<sub>2</sub> lattice with the presence of inter-metallic layer [22]. Increase in Raman peak intensity is also observed similar to XRD results confirming improved crystallinity with increase in Ag layer thickness. Also, the increase in total peak area, calculated upon deconvolution, implies the improvement in short-range atomic ordering and local microstructure upon the increase in Ag thickness [18].

### 3.5 FTIR

Figure 7 presents the FTIR analyses of TiO<sub>2</sub>/Ag/TiO<sub>2</sub> multilayer films done along 400 cm<sup>-1</sup> to 4000 cm<sup>-1</sup> (stacked) to detect the trace of TiO<sub>2</sub>/Ag and functional bonding related to it. The peak at 483 cm<sup>-1</sup> is related to bending vibration (Ti–O–Ti) bonds in TiO<sub>2</sub> lattice [23, 24]. Weak band at 550 cm<sup>-1</sup> relates to transverse optical phonon vibration of Ag–O bond [25]. This Ag–O bond is present only in TiO<sub>2</sub>/Ag/TiO<sub>2</sub> multilayer films but not observed in TiO<sub>2</sub> monolayer film (TAT A) which is in accordance with the experiment. Although, no effect was observed in



**Fig. 4** FESEM image of  $\text{TiO}_2/\text{Ag}/\text{TiO}_2$  multilayer films with the increase in Ag thickness. (a)  $\text{TiO}_2$  monolayer, (b) Ag 2 nm, (c) Ag 4 nm, and (d) Ag 8 nm. Inset image represents the crystallite size estimated by imageJ software

the absorption peak related to the increase in Ag thickness. Ananth et al. (2016) reported the presence of Ag–O metal oxide vibration between 650 and 800  $\text{cm}^{-1}$  but it was not observed in our FTIR spectra. The peak at 775  $\text{cm}^{-1}$  and 939  $\text{cm}^{-1}$  is related to stretching vibrations of Ti–O–Ti and Ti–O bonding, respectively [26]. The inset of Fig. 7 presents the same FTIR spectra (1200 and 4000  $\text{cm}^{-1}$ ) but in high scale for clarity. Peaks at 1433  $\text{cm}^{-1}$ , 2860  $\text{cm}^{-1}$ , 2960  $\text{cm}^{-1}$  are observed due to symmetric and anti-symmetric vibrations of surfactants present in the samples [27]. Peak at 1640  $\text{cm}^{-1}$  represents the bending vibrations of Ti–OH bonding due to chemically absorbed water molecule [24, 28]. Gao et al. (2003) have reported the presence of OH group between 3100 and 3600  $\text{cm}^{-1}$  while Latha et al. reported similar functional group between 3400 and 3600  $\text{cm}^{-1}$  but very weak bonds were observed in our samples in those range [23, 29].

The doublet peak around 2000  $\text{cm}^{-1}$  (inset) may have originated due to instrumental grating error.

### 3.6 UV-Visible

Figure 8a presents UV-Visible spectra (%t) of TAT multilayer films with variation in Ag thickness. TAT multilayers show the transmittance between 65 and 80% at 550 nm wavelength with TAT D being the most optically transmitting film. But in higher wavelength region (1000–2500 nm), the transmittance changes as a parabolic function with TAT A showing the highest transmittance and TAT D lowest. This phenomenon happens due to the scattering of light at Ag and  $\text{TiO}_2$  interface, while absorption of light is due to the electronic transition from 3d to 4s orbitals above Fermi level. But this behavior can only be observed in multilayers with mid-layer thickness

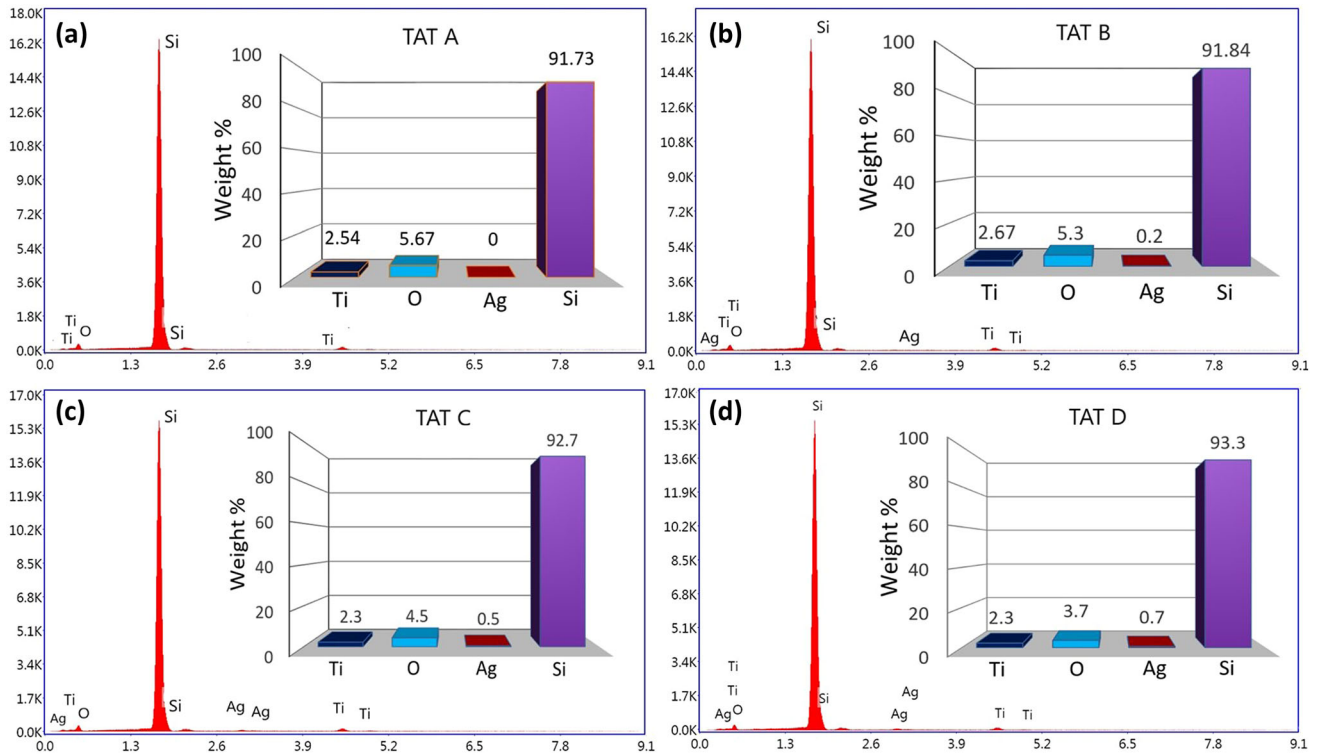


**Fig. 5** EDX elemental composition of Ti and Ag (wt%) in multilayer films with the increase in Ag thickness. (a) TiO<sub>2</sub> monolayer, (b) Ag 2 nm, (c) Ag 4 nm, and (d) Ag 8 nm

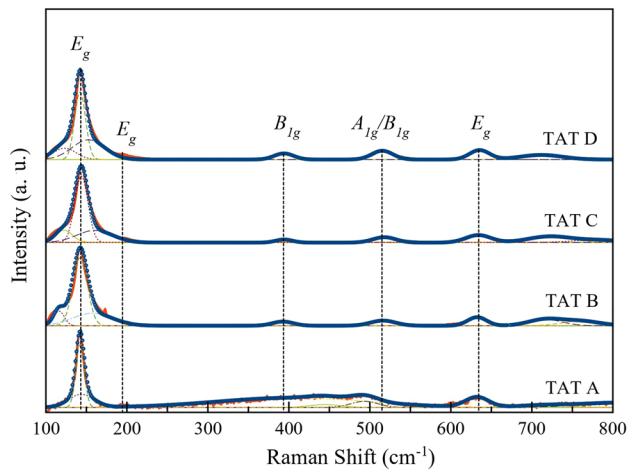


**Fig. 6** Raman spectra of TiO<sub>2</sub>/Ag/TiO<sub>2</sub> multilayer films. Peaks were fitted with Gaussian profile

below 10 nm where Ag islands are discontinuous. These discontinuous islands limit the mean free path of conducting electrons resulting in the decrease in transmittance [30]. The dielectric function depending upon the size of the Ag islands can be given by [31]

$$\epsilon_R = \epsilon_m + \frac{C}{R}, \tag{3}$$

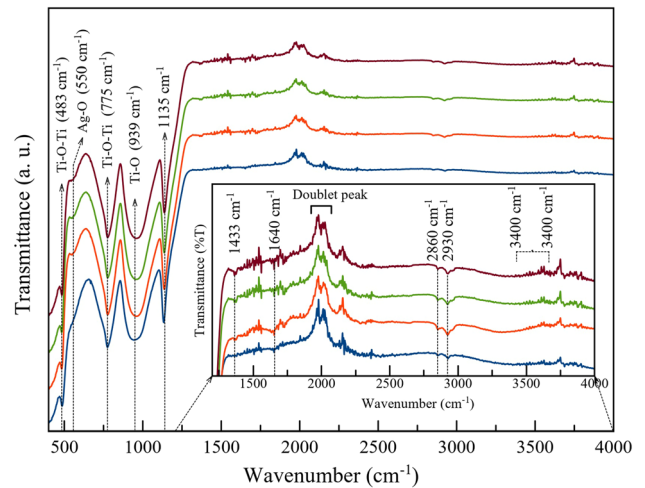


**Fig. 7** FTIR spectra of TiO<sub>2</sub>/Ag/TiO<sub>2</sub> multilayer films scanned from 400 to 4000 cm<sup>-1</sup>. Inset picture represents the scaled-up image of the spectra (1200 to 4000 cm<sup>-1</sup>) for clarity

where  $\epsilon_m$  is dielectric constant,  $R$  is particle radius, and  $C$  is constant. This leads to lower transmittance for smaller Ag islands below a critical value. It is observed that lower Ag mid-layer thickness leads to small discontinuous Ag islands forming below the

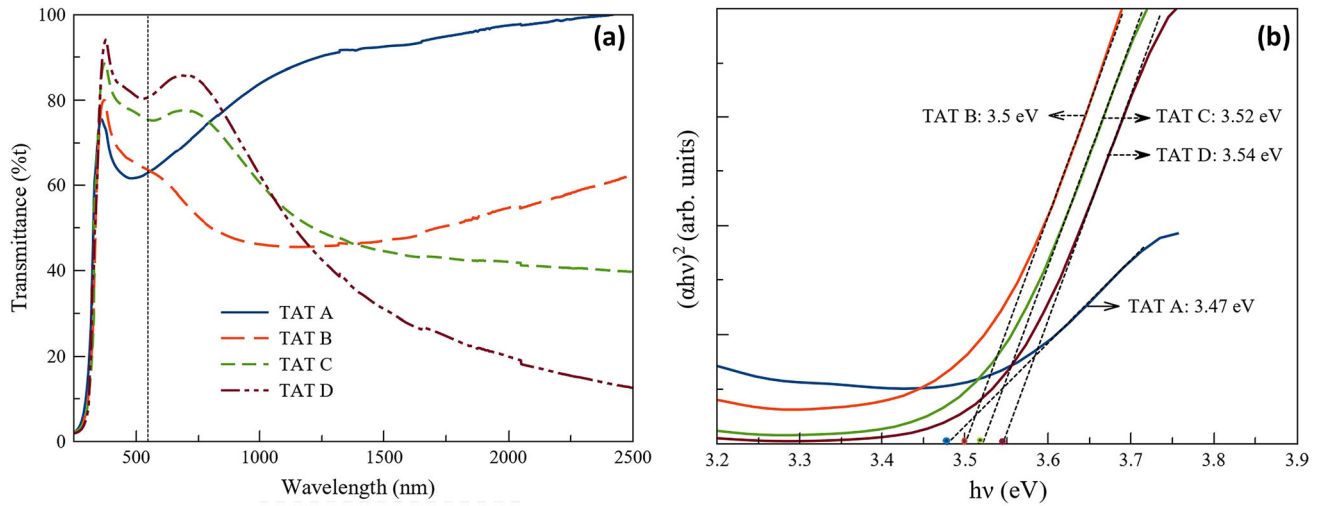


**Fig. 8** (a) UV–Vis spectra of TiO<sub>2</sub>/Ag/TiO<sub>2</sub> multilayer films in transmittance mode as function of mid-layer Ag thickness. (b) Tauc plot of multilayer films for optical band gap calculation

TiO<sub>2</sub> layer. Due to the scattering of light from the TiO<sub>2</sub>/Ag interface, the average transmittance is low (< 80%). The multilayer thin films transmittance is strongly affected by the surface plasmonic effect due to high optical absorption. This results in decrease in average transmittance with small island size from lower Ag thickness. With the increase in Ag thickness above critical value, the continuous islands decrease the light scattering resulting in high transmittance [32].

In visible region, higher transmittance was observed at 700 nm wavelength due to coupling between incident light and surface plasmon of the Ag islands. The decrease in optical transmittance in IR region is observed due to the reflection depending upon surface plasmon absorption. The plasmon frequency ( $\omega_p$ ) can be described from Drude–Lorentz free electron model as

$$\omega_p = \sqrt{\frac{ne^2}{m\epsilon_0}}, \tag{4}$$

where  $n$  is the carrier density and  $\epsilon_0$  is the permittivity in free space [33].

Figure 8b presents the band gap of TAT multilayer films calculated by tauc plot method ranging between 3.47 and 3.54 eV. The shift in band gap of multilayer films is due to the increase in free charge carriers with Ag layer thickness which leads to Burstein–Moss effect [34]. In this effect, free charge carriers fill the states near the bottom of conduction band leading to

shift in Fermi level resulting in the widening of band gap. The shift in Fermi level is given by

$$\Delta E = \frac{h^2}{8m_{VC}^*} \left( \frac{3N}{\pi} \right)^{2/3} \tag{5}$$

So, widening of band gap is calculated by

$$E_0 = E_G + \Delta E, \tag{6}$$

where  $m_{VC}^*$  is the effective mass of conduction and valence band,  $N$  is free electron density,  $E_G$  is the minimum energy separation of thin film band [35].

### 3.7 Electrical properties

Electrical properties of TAT multilayer largely depend upon the highly conductive metallic mid-layer. Sheet resistance, mobility, and carrier concentration are calculated as a factor of Ag layer thickness (Fig. 9). Results from few other authors are important in the discussion for a comparative study. Loka et al. (2017) have reported the decrease in sheet resistance as a factor of  $-3.07$  (slope) with the increase in percentage Ag thickness in TiO<sub>2</sub>/Ag/TiO<sub>2</sub> multilayer (total thickness) from 5.9 to 15.8% [36]. Similarly, the carrier concentration and mobility is reported to be increasing as a factor of 1.12 and 0.48, respectively. Dhar et al. (2013) have reported the decrease in sheet resistance to factor of  $-9.95$  with Ag content from 8.3 to 21.7% [31]. The author has also reported the increase in carrier concentration and mobility as a factor of 1.01 and 1.14, respectively. Kim et al. (2015) have reported similar trend for sheet



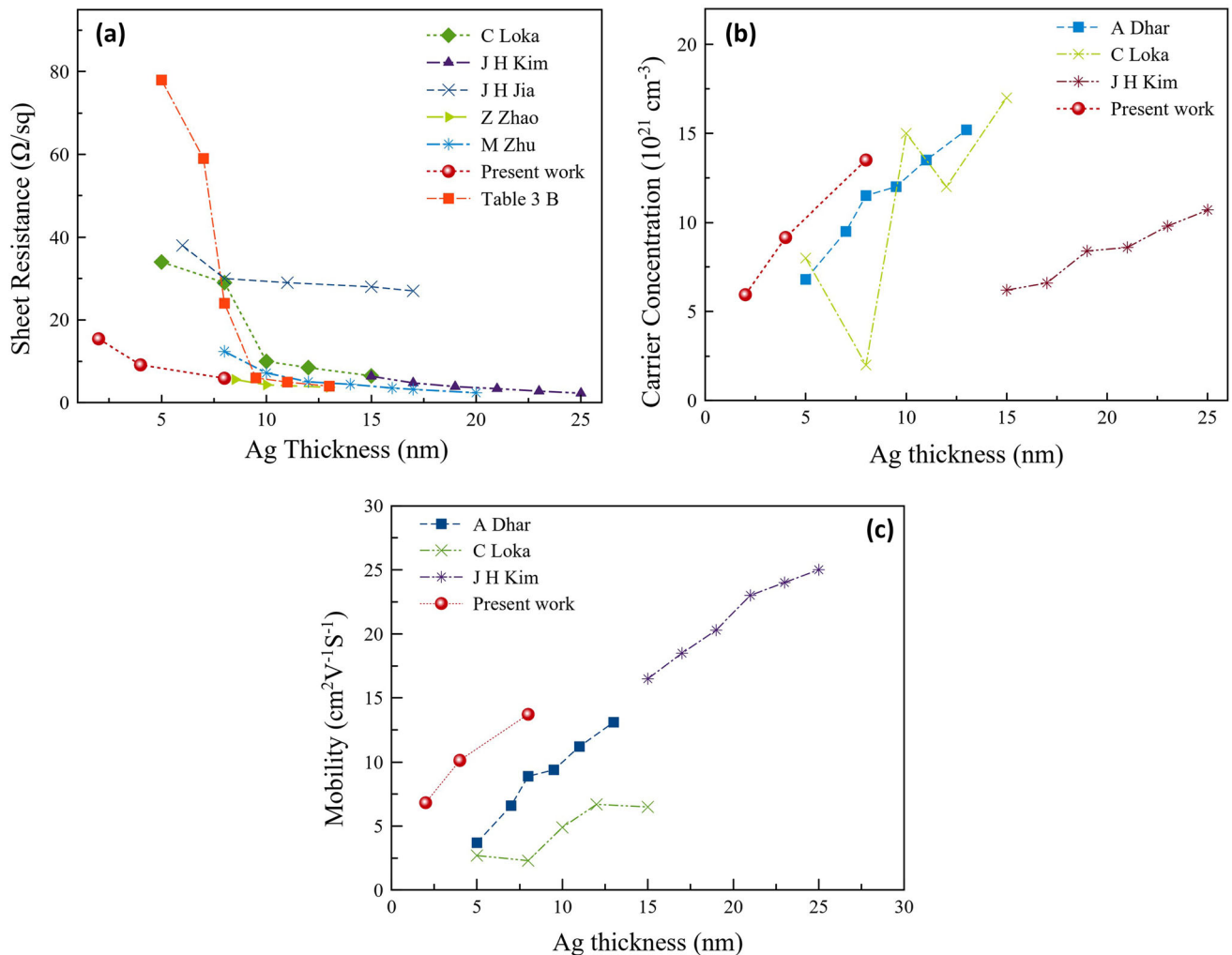


**Fig. 9** (a) Sheet resistance, (b) carrier concentration, and (c) Mobility of TiO<sub>2</sub>/Ag/TiO<sub>2</sub> multilayer films compared with references against the increase in Ag layer thickness

resistance, carrier concentration, and mobility as a factor of  $-0.38$ ,  $0.46$ , and  $0.88$ , respectively, along  $15.8$ – $23.8\%$  Ag content [10]. Jia et al. (2004) have reported similar trend in sheet resistance with a factor of  $-0.78$  with Ag content from  $23.1$  to  $45.9\%$  [37]. The high mid-layer Ag thickness ( $6$ – $17$  nm) between  $10$ -nm-thick TiO<sub>2</sub> does not show a sharp drop in sheet resistance rather a very low decreasing rate. Zhu et al. (2016) have reported similar decline in sheet resistance with factor of  $-0.732$  along  $11.8$ – $25\%$  Ag thickness [38]. This work reports the decrease in sheet resistance from  $15.4$  to  $5.92$  Ω/□ as a factor of  $-1.47$  from percentage Ag thickness of  $6.3$ – $14.3\%$ . Carrier concentration varies from  $5.94 \times 10^{21}$  to  $1.35 \times 10^{22}$  cm<sup>-3</sup>, whereas mobility varies from  $6.8$  to  $13.7$  cm<sup>2</sup> V<sup>-1</sup> S<sup>-1</sup> with a factor of  $1.23$  and  $1.11$ , respectively.

It is observed that conduction through the dielectric dominates below critical Ag thickness forming the discontinuous islands. With the increase in island size and Ag thickness, decrease in resistivity is observed due to quantum tunneling between the island gaps. The conductivity ( $\sigma$ ) in lower Ag island condition is expressed by the equation

$$\sigma \propto \exp\left(-2\beta L - \frac{W}{k_{\beta}T}\right), \quad (7)$$

where  $W$  denotes the charging energy of Ag island,  $L$  is island separation,  $\beta$  is the tunneling exponent of electron wave functions in the insulator,  $k$  is the Boltzmann constant, and  $T$  is the temperature. With the increase in Ag thickness, the island forms a uniform layer. In this case, the conductivity in multilayer film is derived by the combination of carrier

concentration and mobility of conducting electrons due to surface boundary scattering. The conductivity in this case is given by

$$\frac{\sigma}{\sigma_0} \propto \frac{3}{4}(1-p)k \log \frac{1}{k}, \quad (8)$$

where  $p$  is the electron distribution function at surface,  $\sigma_0$  is conductivity of bulk material,  $k = t/\lambda_0$  [31, 39]. Haacke's figure of merit (FOM) was calculated by the formula:

$$\varphi_{TC} = \frac{T^{10}}{R_S}, \quad (9)$$

where  $T$  is Transmittance and  $R_S$  is sheet resistance. TAT D multilayer with Ag thickness 8 nm gives the best figure of merit with  $7.9 \times 10^{-3} \Omega^{-1}$  [40].

## 4 Conclusion

TiO<sub>2</sub>/Ag/TiO<sub>2</sub> multilayer films were deposited using ion-beam sputtering technique with mid-layer Ag thickness as 2 nm, 4 nm, 8 nm, while TiO<sub>2</sub> thickness is 60 nm. XRR analysis showed the increase in both roughness and densities of multilayer with the increase in Ag thickness. XRD analyses confirmed the presence of both TiO<sub>2</sub> (anatase) and Ag in multilayer films with preferential growth in [101] and [200] planes, respectively. Crystallite size is in multilayers compared to TiO<sub>2</sub> monolayer. The crystallite size of both TiO<sub>2</sub> and Ag increased while micro-strain and dislocation density decreased with the increase in Ag thickness. A lattice mismatch between quartz substrate and multilayer film is also observed giving rise to sharp peak at lower  $2\theta$  value. FESEM images confirm dense, smooth, and crack-free films. Ag islands were visible as dark spots over surface in 4 and 8 nm Ag films. EDX analyses confirmed the presence of TiO<sub>2</sub> and Ag in our films. The composition (wt%) of Ag ranged between 2.5 and 10.3% by volume. Raman spectra confirmed TiO<sub>2</sub> anatase phase with 6 Raman active modes detected in the films, and their intensities increased with Ag thickness confirming crystalline nature of multilayer films. Blue shift of  $E_g$  band in multilayers confirmed phonon confinement effect due to the increase in Ag mid-layer thickness. FTIR detected the presence of Ag–O bond at  $550 \text{ cm}^{-1}$  confirming the presence of Ag in multilayer films. UV-Visible results showed transmittance ranging between 65 and 81% in visible

region (550 nm) and band gap was calculated to be 3.47–3.54 eV for TAT multilayer films. Sheet resistance of TAT multilayers decreased with Ag thickness while carrier concentration and mobility increased with Ag thickness. TAT D with 8 nm Ag thickness showed lowest sheet resistance of  $5.92 \Omega/\square$  with carrier concentration  $1.35 \times 10^{22} \text{ cm}^{-3}$  and mobility  $13.72 \text{ cm}^2/\text{Vs}$ . Haacke's Figure of Merit (FOM) was recorded highest for TAT D to be  $7.9 \times 10^{-3} \Omega^{-1}$  at 8 nm Ag thickness. A well-matched comparative plot of electrical properties with other previous reported data is presented in the manuscript. Optical and electrical properties have further room of improvement by optimal selection of TiO<sub>2</sub> and Ag thickness including other deposition parameters for an optimal TCO. These findings may help in the growth of high-performance TCOs for many future applications.

## Author contributions

All authors contributed to the study conception and design. Material preparation, data collection, and analysis were performed by RS. The first draft of the manuscript was written by SKM and all authors commented on previous versions of the manuscript. All authors read and approved the final manuscript.

## Funding

This work is supported by UGC-DAE CSR Indore, India with Grant no CSRIC/CRS-88/2018-19/1360.

## Data availability

The datasets generated during and/or analyzed during the current study are available from the corresponding author on reasonable request.

## Declarations

**Conflict of interest** We wish to confirm that there are no known conflicts of interest associated with this publication and there has been no significant financial support for this work that could have influenced its outcome.

## References

1. S. Goktas, A. Goktas, A comparative study on recent progress in efficient ZnO based nanocomposite and heterojunction photocatalysts: A review. *J. Alloys Compd.* (2021). <https://doi.org/10.1016/j.jallcom.2021.158734>
2. F.A. Tantray, A. Agrawal, M. Gupta, J.T. Andrews, P. Sen, Effect of oxygen partial pressure on the structural and optical properties of ion beam sputtered TiO<sub>2</sub> thin films. *Thin Solid Films* **619**, 86–90 (2016). <https://doi.org/10.1016/j.tsf.2016.10.020>
3. S. Chao, W.-H. Wang, M.-Y. Hsu, L.-C. Wang, Characteristics of ion-beam-sputtered high-refractive-index TiO<sub>2</sub>-SiO<sub>2</sub> mixed films. *J. Opt. Soc. Am. A* **16**, 1477 (1999). <https://doi.org/10.1364/josaa.16.001477>
4. I.W. Hamley, J.S. Pedersen, Analysis of neutron and X-ray reflectivity data. I. Theory. *J. Appl. Crystallogr.* **27**, 29–35 (1994). <https://doi.org/10.1107/S0021889893006260>
5. S. Festersen, S.B. Hrkac, C.T. Koops, B. Runge, T. Dane, B.M. Murphy, O.M. Magnussen, X-ray reflectivity from curved liquid interfaces. *J. Synchrotron Radiat.* **25**, 432–438 (2018). <https://doi.org/10.1107/S1600577517018057>
6. R. Singh, M. Gupta, D.M. Phase, S.K. Mukherjee, Phase growth analysis of sputtered TiO<sub>2</sub> thin films at low oxygen partial pressures using XANES and XRR. *Mater. Res. Express.* **6**, 116449 (2019). <https://doi.org/10.1088/2053-1591/ab4e3f>
7. L.G. Parratt, Surface studies of solids by total reflection of X-rays. *Phys. Rev.* **95**, 359–369 (1954). <https://doi.org/10.1103/PhysRev.95.359>
8. A.L. Patterson, The Scherrer formula for X-ray particle size determination. *Phys. Rev.* **56**, 978–982 (1939). <https://doi.org/10.1103/PhysRev.56.978>
9. A. Khorsand Zak, W.H. Abd Majid, M.E. Abrishami, R. Yousefi, X-ray analysis of ZnO nanoparticles by Williamson-Hall and size-strain plot methods. *Solid State Sci.* **13**, 251–256 (2011). <https://doi.org/10.1016/j.solidstatesciences.2010.11.024>
10. J.H. Kim, D.H. Kim, T.Y. Seong, Realization of highly transparent and low resistance TiO<sub>2</sub>/Ag/TiO<sub>2</sub> conducting electrode for optoelectronic devices. *Ceram. Int.* **41**, 3064–3068 (2015). <https://doi.org/10.1016/j.ceramint.2014.10.148>
11. N.A. Shah, A. Nazir, W. Mahmood, W.A.A. Syed, S. Butt, Z. Ali, A. Maqsood, Physical properties and characterization of Ag doped CdS thin films. *J. Alloys Compd.* **512**, 27–32 (2012). <https://doi.org/10.1016/j.jallcom.2011.08.081>
12. H. Gencer, M. Gunes, A. Goktas, Y. Babur, H.I. Mutlu, S. Atalay, LaBaMnO films produced by dip-coating on a quartz substrate. *J. Alloys Compd.* **465**, 20–23 (2008). <https://doi.org/10.1016/j.jallcom.2007.10.110>
13. A. Goktas, S. Modanlı, A. Tumbul, A. Kilic, Facile synthesis and characterization of ZnO, ZnO:Co, and ZnO/ZnO: Co nano rod-like homojunction thin films: Role of crystallite/grain size and microstrain in photocatalytic performance. *J. Alloys Compd.* **893**, 162334 (2022). <https://doi.org/10.1016/j.jallcom.2021.162334>
14. P. MuhammedShafi, A. ChandraBose, Impact of crystalline defects and size on X-ray line broadening: A phenomenological approach for tetragonal SnO<sub>2</sub> nanocrystals. *AIP Adv.* **5**, 57137 (2015). <https://doi.org/10.1063/1.4921452>
15. T. Müller, H. Nienhaus, Ultrathin Ag films on H:Si(111)-1×1 surfaces deposited at low temperatures. *J. Appl. Phys.* **93**, 924–929 (2003). <https://doi.org/10.1063/1.1530714>
16. K.A. Lozovoy, A.G. Korotaev, A.P. Kokhanenko, V.V. Dirko, A.V. Voitsekhovskii, Kinetics of epitaxial formation of nanostructures by Frank–van der Merwe, Volmer–Weber and Stranski–Krastranow growth modes. *Surf. Coatings Technol.* **384**, 125289 (2020). <https://doi.org/10.1016/j.surfcoat.2019.125289>
17. H. Ferhati, F. Djeflal, N. Martin, Highly improved responsivity of self-powered UV–Visible photodetector based on TiO<sub>2</sub>/Ag/TiO<sub>2</sub> multilayer deposited by GLAD technique: Effects of oriented columns and nano-sculptured surface. *Appl. Surf. Sci.* **529**, 35–38 (2020). <https://doi.org/10.1016/j.apsusc.2020.147069>
18. S.K. Mukherjee, D. Mergel, Thickness dependence of the growth of magnetron-sputtered TiO<sub>2</sub> films studied by Raman and optical transmittance spectroscopy. *J. Appl. Phys.* (2013). <https://doi.org/10.1063/1.4811682>
19. J. Kulczyk-Malecka, P.J. Kelly, G. West, G.C.B. Clarke, J.A. Ridealgh, K.P. Almtoft, A.L. Greer, Z.H. Barber, Investigation of silver diffusion in TiO<sub>2</sub>/Ag/TiO<sub>2</sub> coatings. *Acta Mater.* **66**, 396–404 (2014). <https://doi.org/10.1016/j.actamat.2013.11.030>
20. A. Chanda, K. Rout, M. Vasundhara, S.R. Joshi, J. Singh, Structural and magnetic study of undoped and cobalt doped TiO<sub>2</sub> nanoparticles. *RSC Adv.* **8**, 10939–10947 (2018). <https://doi.org/10.1039/c8ra00626a>
21. W.F. Zhang, Y.L. He, M.S. Zhang, Z. Yin, Q. Chen, Raman scattering study on anatase TiO<sub>2</sub> nanocrystals. *J. Phys. D* **33**, 912–916 (2000). <https://doi.org/10.1088/0022-3727/33/8/305>
22. I. Olvera-Rodríguez, R. Hernández, A. Medel, C. Guzmán, L. Escobar-Alarcón, E. Brillas, I. Sirés, K. Esquivel, TiO<sub>2</sub>/Au/TiO<sub>2</sub> multilayer thin-film photoanodes synthesized by pulsed laser deposition for photoelectrochemical degradation of organic pollutants. *Sep. Purif. Technol.* **224**, 189–198 (2019). <https://doi.org/10.1016/j.seppur.2019.05.020>

23. H.K.E. Latha, H.S. Lalithamba, Synthesis and characterization of titanium dioxide thin film for sensor applications. *Mater. Res. Express.* (2018). <https://doi.org/10.1088/2053-1591/aab695>
24. P. Praveen, G. Viruthagiri, S. Mugundan, N. Shanmugam, Structural, optical and morphological analyses of pristine titanium di-oxide nanoparticles—Synthesized via sol-gel route. *Spectrochim. Acta A Mol. Biomol. Spectrosc.* **117**, 622–629 (2014). <https://doi.org/10.1016/j.saa.2013.09.037>
25. A. Ananth, Y.S. Mok, Dielectric barrier discharge (DBD) plasma assisted synthesis of Ag<sub>2</sub>O nanomaterials and Ag<sub>2</sub>O/RuO<sub>2</sub> nanocomposites. *Nanomaterials* (2016). <https://doi.org/10.3390/nano6030042>
26. S.H. Nam, S.J. Cho, J.H. Boo, Growth behavior of titanium dioxide thin films at different precursor temperatures. *Nanoscale Res. Lett.* **7**, 1–6 (2012). <https://doi.org/10.1186/1556-276X-7-89>
27. Y. Bouachiba, F. Hanini, A. Bouabellou, F. Kermiche, A. Taabouche, M. Bouafia, S. Amara, S. Sahli, K. Boukheldaden, TiO<sub>2</sub> thin films studied by FTIR, AFM and spectroscopic ellipsometry. *Int. J. Nanopart.* **6**, 169–177 (2013). <https://doi.org/10.1504/IJNP.2013.054992>
28. T. Ali, A. Ahmed, U. Alam, I. Uddin, P. Tripathi, M. Muneer, Enhanced photocatalytic and antibacterial activities of Ag-doped TiO<sub>2</sub> nanoparticles under visible light. *Mater. Chem. Phys.* **212**, 325–335 (2018). <https://doi.org/10.1016/j.matchemphys.2018.03.052>
29. Y. Gao, Y. Masuda, Z. Peng, T. Yonezawa, K. Koumoto, Room temperature deposition of a TiO<sub>2</sub> thin film from aqueous peroxotitanate solution. *J. Mater. Chem.* **13**, 608–613 (2003). <https://doi.org/10.1039/b208681f>
30. K. Sivaramakrishnan, T.L. Alford, Conduction and transmission analysis in gold nanolayers embedded in zinc oxide for flexible electronics. *Appl. Phys. Lett.* **96**, 2008–2011 (2010). <https://doi.org/10.1063/1.3435467>
31. A. Dhar, T.L. Alford, High quality transparent TiO<sub>2</sub>/Ag/TiO<sub>2</sub> composite electrode films deposited on flexible substrate at room temperature by sputtering. *APL Mater.* (2013). <https://doi.org/10.1063/1.4808438>
32. K. Sivaramakrishnan, T.L. Alford, Metallic conductivity and the role of copper in ZnO/Cu/ZnO thin films for flexible electronics. *Appl. Phys. Lett.* (2009). <https://doi.org/10.1063/1.3077184>
33. P. Wang, D. Zhang, D.H. Kim, Z. Qiu, L. Gao, R.I. Murakami, X. Song, Enhancement of light transmission by coupling to surface plasmon polaritons of a layer-plus-islands silver layer. *J. Appl. Phys.* **106**, 10–15 (2009). <https://doi.org/10.1063/1.3259426>
34. E. Burstein, Anomalous optical absorption limit in InSb [4]. *Phys. Rev.* **93**, 632–633 (1954). <https://doi.org/10.1103/PhysRev.93.632>
35. E.R. Rwenyagila, B. Agyei-Tuffour, M.G. Zebaze Kana, O. Akin-Ojo, W.O. Soboyejo, Optical properties of ZnO/Al/ZnO multilayer films for large area transparent electrodes. *J. Mater. Res.* **29**, 2912–2920 (2014). <https://doi.org/10.1557/jmr.2014.298>
36. C. Loka, K.S. Lee, Preparation of TiO<sub>2</sub>/Ag/TiO<sub>2</sub> (TAT) multilayer films with optical and electrical properties enhanced by using Cr-added Ag film. *Appl. Surf. Sci.* **415**, 35–42 (2017). <https://doi.org/10.1016/j.apsusc.2016.11.082>
37. J.H. Jia, P. Zhou, H. Xie, H.Y. You, J. Li, L.Y. Chen, Study of optical and electrical properties of TiO<sub>2</sub>/Ag/TiO<sub>2</sub> multilayers. *J. Korean Phys. Soc.* **44**, 717–721 (2004). <https://doi.org/10.3938/jkps.44.717>
38. M.Q. Zhu, H.D. Jin, P.Q. Bi, F.J. Zong, J. Ma, X.T. Hao, Performance improvement of TiO<sub>2</sub>/Ag/TiO<sub>2</sub> multilayer transparent conducting electrode films for application on photodetectors. *J. Phys. D* **49**, 115108 (2016). <https://doi.org/10.1088/0022-3727/49/11/115108>
39. M. Wu, S. Yu, L. He, L. Yang, W. Zhang, High quality transparent conductive Ag-based barium stannate multilayer flexible thin films. *Sci. Rep.* **7**, 1–9 (2017). <https://doi.org/10.1038/s41598-017-00178-9>
40. G. Haacke, New figure of merit for transparent conductors. *J. Appl. Phys.* **47**, 4086–4089 (1976). <https://doi.org/10.1063/1.323240>

**Publisher's Note** Springer Nature remains neutral with regard to jurisdictional claims in published maps and institutional affiliations.